Competing multiple-q magnetic structures in HoGe$_3$: I. The magnetic phase diagram of HoGe$_3$

Competing multiple-q magnetic structures in HoGe₃: I. The magnetic phase diagram of HoGe₃

P Schobinger-Papamantellos[1]**, J Rodríguez-Carvajal**[2]**, L D Tung**[3]**,
C Ritter**[2] **and K H J Buschow**[4]

[1] Laboratory of Crystallography, ETH-Zurich, 8093 Zürich, Switzerland
[2] Institut Laue-Langevin, 156X, 38042 Grenoble Cédex, France
[3] Department of Physics, University of Liverpool, L69 7ZE, UK
[4] Van der Waals-Zeeman Institute, University of Amsterdam, NL-1018 XE,
Amsterdam, The Netherlands

E-mail: Schobinger@mat.ethz.ch and JRC@ill.fr

Abstract
The magnetic phase diagram of the antiferromagnetic HoGe₃ compound (space group
$Cmcm$, $Z = 4$, $T_N = 11$ K) has been investigated by means of magnetic measurements,
specific heat and high resolution neutron powder diffraction. The specific heat and the magnetic
measurements display anomalies at $T_N = 11$ K and indicate minor transitions at $T_1 = 9.5$ K
$T_2 = 8.1$ K and $T_3 = 4.8$ K (on heating). The neutron data in terms of wavevectors show three
distinct regions of magnetic ordering with two multiple-q competing magnetic structures and
several transitions, besides the paramagnetic state: (i) the high temperature (HT) range
$T_2 \rightarrow T_N$ is described with the wavevectors (q_1, q_2), $q_1 = (q_{1x}, 0, 0)$ with $q_{1x} \approx \frac{1}{2}$ and
$q_2 = (q_{2x}, 0, q_{2z})$ with $q_{2x} \approx \frac{1}{2}$ and $q_{2z} \approx \frac{1}{3}$ and T dependent length, and the presence of q_1
below T_1 is not fully confirmed unlike the case for isomorphic TbGe₃; (ii) the low temperature
range (LT) 1.5 K $\rightarrow T_2$ is described with the wavevectors (q_3, q_4) with $q_3 = (\frac{1}{2}, q_{3y}, 0)$,
$q_4 = (\frac{1}{2}, q_{4y}, \frac{1}{3})$, and subdivides into the lock-in LT₁ range 1.5 K$\rightarrow T_3$ where $q_{3y} = q_{4y} = \frac{1}{4}$
have a constant length and the LT₂ range $T_3 \rightarrow T_2$ where q_{3y} and q_{4y} have a length variable
with T; (iii) the intermediate temperature range refers to the range of coexistence of the two
structures as metastable phases in varying proportions around the first-order transition T_2.
Between the vectors (q_1, q_2) and (q_3, q_4) describing the HT and the LT phases there is no
simple (group–subgroup) symmetry relation and the transition between them at T_2 is of first
order (hysteresis effects). Part I of the paper focuses on the model independent analysis of
various sets of neutron data that lead to a rather complex magnetic phase diagram. A model
dependent description and refinements of the underlying multiple-q magnetic structures will be
given in part II.

(Some figures in this article are in colour only in the electronic version)

1. Introduction

Since the discovery of the novel DyGe₃ [1] structure type
in the corresponding germanium richest heavy rare earth
(R) compound and in the isomorphic RGe₃ (R = Tb, Dy,
Ho, Er and Y) compounds, the magnetic ordering and
magnetic structures formed in these compounds [2–5] have
been investigated in several studies, on the basis of magnetic

measurements and neutron diffraction, by us and other
researchers. It follows from these studies that their magnetic
structure is far from uniform, as already reported for the parent
CrB type RGe compounds [6]. In fact the RGe₃ structure is a
stacking variant of the CrB type structure with the change of
the stacking sequence along the longest axis b of introducing
4 Ge atomic layers perpendicular to it that lead to a doubling in
length of this axis. The building blocks of the CrB structure are

trigonal rare earth prisms centred with Ge/Si, which are stacked in a double-layer arrangement parallel to the pseudo-tetragonal (010) plane with the trigonal prism axis along a. The RGe$_3$ and RGe compounds have the same space group $Cmcm$ and comparable a and c lattice parameters while $b_{RGe_3} \approx 2b_{RGe}$.

Non-magnetic YGe$_3$ was reported to become superconducting at 2.2 K [7, 8] while the compounds with a magnetic rare earth RGe$_3$ (R = Tb, Dy, Ho, Er) order antiferromagnetically with T_N of 40 K, 24 K, 12 K, 7 K respectively within the series. On the basis of band structure calculations DyGe$_3$ was reported to be a two-dimensional conductor [9] perpendicular to the b axis. A wealth of different antiferromagnetic structure types and phase transitions are displayed, ranging from collinear antiferromagnetism within the (a, b) plane in ErGe$_3$ ($q = 0$), to multiple-q vector structures in DyGe$_3$ and TbGe$_3$. The ordering of DyGe$_3$ is associated with a three-times cell enlargement $(2a, b, 3c)$ referring to the basis cell P, or alternatively with two wavevectors $q_1 = (\frac{1}{2}, 0, 0)$ and $q_2 = (\frac{1}{2}, 0, \frac{1}{3})$ of the same basis P. At high temperatures (HT) the magnetic structure corresponds to a uniaxial antiphase domain structure with two amplitudes that square up at low temperatures (LT) to a constant moment structure with a ferrimagnetic stacking $(+ + -)$ along c and anti-translation $(+-)$ along a.

TbGe$_3$ displays a more complex behaviour, comprising incommensurate multiple-q vector canted structures with two symmetry independent vectors $q_1 = (q_{1x}, 0, 0)$ and $q_2 = (q_{2x}, 0, q_{2z})$ with $q_{1x} \neq q_{2x} \approx \frac{1}{2}$, $q_{2z} \approx \frac{1}{3}$. In the HT regime from $T_{ic} = 24$ K to $T_N = 40$ K the action of the two wavevectors in physical space results in planar incommensurate moment arrangements, corresponding to a fluctuating canted magnetic structure. In this context the term 'fluctuating' means that, within the plane (b, c), both the moment orientation and the moment size are position dependent. Furthermore a spin reorientation transition occurs at lower temperatures simultaneously with a lock-in transition towards a squared-up antiphase domain uniaxial structure with a six-times larger cell $(2a, b, 3c)$ with $q_1 = (\frac{1}{2}, 0, 0)$ and $q_2 = (\frac{1}{2}, 0, \frac{1}{3})$ referring to the non-primitive cell C at variance with the case of DyGe$_3$ (P-cell).

Among the RGe$_3$ compounds however, HoGe$_3$ showed the most complex behaviour; the magnetic structure has remained unresolved until now. In a preliminary neutron diffraction study the first attempt to index the HoGe$_3$ (sample I) LT neutron patterns led to a 40-times cell enlargement $(5a, 2b, 4c)$ of the orthorhombic $Cmcm$ ($Z = 4$, all atoms at 4c $(0, y, \frac{1}{4})$, $a = 4.04$ Å, $b = 20.79$ Å, $c = 3.91$ Å) cell, which exceeds the limits of neutron powder diffraction. In such cases it should be noted that, on the one hand, the usual procedure of symmetry analysis for parameter reduction does not apply, as the symmetry gets lost, and on the other hand, the number of independent experimental observations is strongly reduced due to exceeding peak overlap in powder diffraction.

The present paper focuses on the magnetic ordering of HoGe$_3$ by enlarging the experimental basis with high resolution neutron data collected with a narrow temperature window and with the help of new software developed in the meantime. To ensure that the LT pattern complexity was not sample dependent the data were collected for a second sample
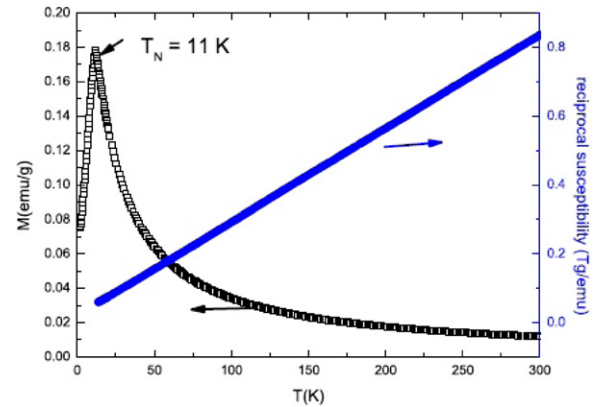

Figure 1. Temperature dependence of the magnetization M (left scale) and temperature dependence of the reciprocal susceptibility (χ^{-1}, right scale) of HoGe$_3$. The data were obtained in a field of 0.1 kOe.

(II) synthesized under similar conditions. We will show that a numerical analysis of this complex situation associated with cell enlargements could be found in an intuitive way. Of important help was the experience accumulated working on the recently published TbGe$_3$ incommensurate canted phases [5] that offered the first approach to the HT HoGe$_3$ ordering.

The use of various neutron powder diffraction data sets (high intensity (HI) data on heating and cooling and high resolution (HR) data on heating) in the analyses of the following sections arises from the nature of the problem displaying competing magnetic structures and the concomitant phase transitions. The paper is separated into two parts with respect the neutron diffraction data analysis.

Part I relates to the physical properties and the extraction of *the model independent information* from neutron diffraction data 4.1. It covers the structural refinements from HR neutron data 4.1.1, the magnetic phase transitions 4.1.2, the indexing 4.1.3, thermal behaviour of the magnetic satellites 4.1.4 and finally the magnetic phase diagram 5.

Part II deals with the *model dependent analyses* of the neutron data as regards the magnetic ordering.

2. Sample preparation

The HoGe$_3$ sample (II) was prepared by arc melting of the appropriate amounts of holmium and germanium in an atmosphere of purified argon gas. The purity of the starting materials was 99.9% for holmium and 99.99% for germanium. After arc melting, the sample was vacuum annealed in a quartz tube for a month at 800 °C. Standard x-ray diffraction using Cu Kα radiation shows that the annealed sample is single phase.

3. Magnetic and specific heat measurements

The magnetic properties of HoGe$_3$ are studied by means of susceptibility and magnetization and specific heat measurements; cf figures 1–4.
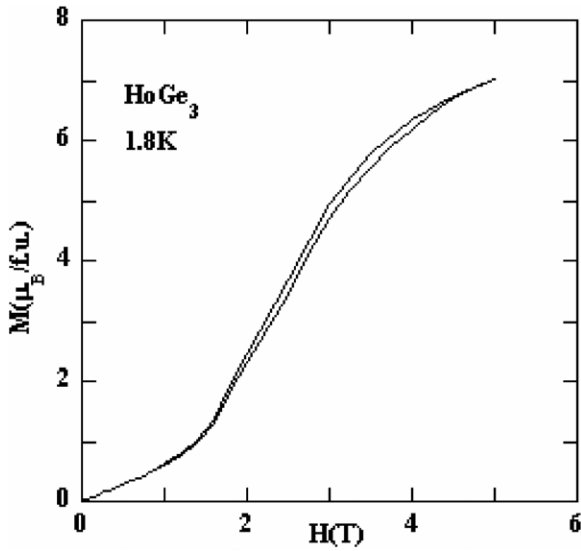
Figure 2. Field dependence $M(H)$ of the magnetization of HoGe$_3$ at 1.8 K showing a first-order metamagnetic transition.
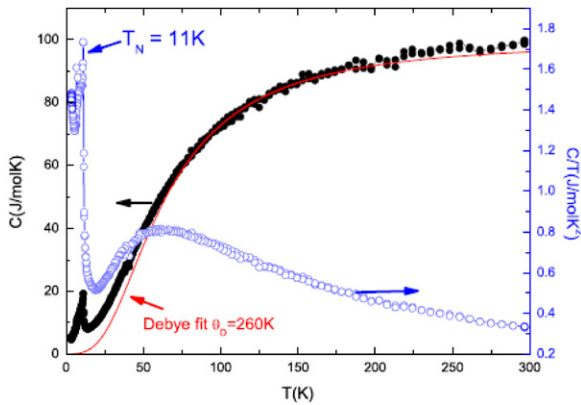

Figure 3. Temperature dependence of the specific heat on cooling (left scale) and of C/T versus T (right scale).

3.1. Magnetization

The bulk magnetic properties were measured using a SQUID magnetometer in the temperature range $1.8 \rightarrow 300$ K. Results obtained for the temperature and field dependence of the magnetization are shown in figures 1 and 2, respectively. Curie–Weiss behaviour of the reciprocal susceptibility (χ^{-1}) is observed down to the lowest temperatures, about 15 K; see figure 1. From the slope and the intercept with the horizontal axis of the reciprocal susceptibility curve we derive an effective moment of $\mu_{\mathrm{eff}} = 10.80\ \mu_{\mathrm{B}}$/Ho atom and an asymptotic Curie–Weiss intercept of $\theta p = -7.68$ K. The value of μ_{eff} obtained is slightly higher than that of $10.61 \mu_{\mathrm{B}}$ expected for trivalent Ho^{3+} ions.

The temperature dependence of the magnetization (M) shows a peak centred at $T_{\mathrm{N}} = 11$ K, indicating antiferromagnetic ordering below this temperature. The data given in figure 1 are measured with a temperature step of 0.5 K in the low temperature range $T < 30$ K (on heating). More precise data are collected with a 0.1 K temperature step on
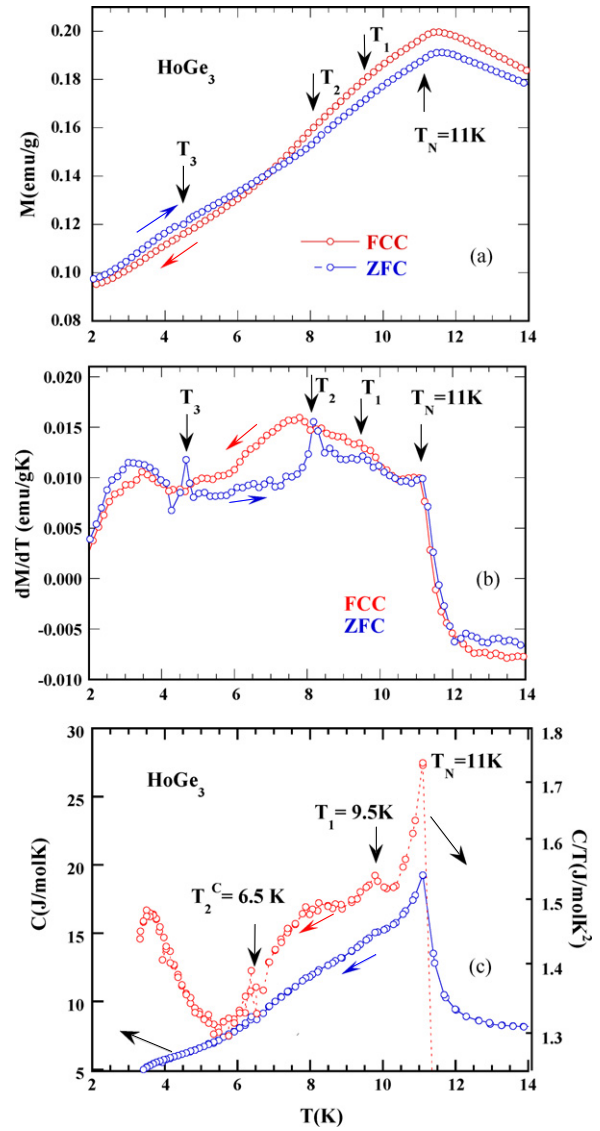

Figure 4. (a) A part of the low temperature dependence of the magnetization M of HoGe$_3$. The data were obtained in a field of 0.1 kOe and with a temperature step of 0.1 K in the range $1.8\ \mathrm{K} \rightarrow 30$ K on heating (ZFC) and cooling (FCC). The vertical arrows indicate the temperatures found in figure 4(b). (b) Magnetic transitions around $T_1 = 9.5$ K, $T_2 = 8.1$ K and $T_3 = 4.8$ K observed in the heating curve of the derivative dM/dT versus T of the low temperature magnetization (figure 4(a)). The larger hysteresis between heating and cooling is found just below the first-order transition T_2. (c) The low temperature dependence of the specific heat (left scale) and of C/T (right scale) showing two anomalies at $T_{\mathrm{N}} = 11$ K and a minor anomaly below 9.5 K (on cooling). A third anomaly around 6.6 K in the C/T (right scale) is assigned to the T_2^{C} temperature.

cooling and heating in the LT range $1.5\ \mathrm{K} \rightarrow 30$ K. These data indicate the existence of three further subtle anomalies and are compared below with the results for the specific heat in figure 4.

In the antiferromagnetic regime, the magnetic moments appear weakly coupled and the compound can be easily transformed to the forced ferromagnetic regime through the metamagnetic transition in a relatively weak field of about 2 T (figure 2). The slight hysteresis indicates that the metamagnetic

transition is of first order. At 5 T the value of the magnetization obtained at 1.8 K is of about 7 μ_B/Ho atom compared with the theoretical full moment value of the Ho^{3+} free ion, $gJ = 10.0\ \mu_B$. The absence of saturation at 5 T may indicate the existence of antiferromagnetic components.

3.2. Specific heat

The heat capacity measurements were made in the temperature range from 2 to 300 K (on cooling) using a Quantum Design Physical Property Measurement System (PPMS) with a heat capacity option. A general view figure of the specific heat is given in figure 3 while the low temperature behaviour is shown in figure 4 together with that of the magnetization (on cooling and heating). At high enough temperature ($T > 80$ K), the heat capacity can be fitted using Debye functions which yield a Debye temperature of about 260 K. On the C/T versus T curve one can see a broad peak around 50 K, which can be attributed to the Schottky anomaly arising from the crystal field effect experienced by the Ho atoms. At lower temperature there is a sharp peak that appeared at 11 K due to the antiferromagnetic ordering transition of the compound which was also seen in the magnetization measurements. However, from the heat capacity and the C/T data in figure 4(c), some minor additional anomalies in the spin ordering regime are visible below T_N. The first one is at about $T_1 = 9.5$ K and the second at $T_2^C \approx 6.6$. The symbol T_2^C used here points to first-order character of this transition discussed in the later sections, the superscript C referring to results obtained on cooling. At first viewing, these transitions appear to be absent in the magnetization data on heating (FCC) and cooling (ZFC); see figure 4(a). Instead tiny changes become visible, mainly in the heating curve, around $\approx$4.5 and $\approx$8.1 K. These transitions are better detected when one takes the derivative curves dM/dT (T) of the magnetization. Thus in figure 4(b) besides T_N three small humps become visible at $T_1 = 9.5$ K on heating and cooling and at $T_2^H = 8.1$ K and $T_3 = 4.8$ K (mainly visible on the heating curve). Again the use of the T_2^H symbol points to the first-order character of the T_2 transition, the superscript H referring to results obtained on heating. An indication of the first-order character of the T_2 transition might be sought in the large hysteresis between the FCC and ZFC curves observed below $T_2^H = 8.1$ K in figure 4(b). On the other hand, the nature of the various transitions displayed in figures 4(b) and (c) cannot be explained and assigned to a particular magnetic or crystal structure change on a microscopic scale. For this reason, although the transition temperatures obtained are used to schedule our neutron diffraction data collection, the more reliable transition temperatures and details of the phase diagram are extracted from the analysis of neutron data in terms of wavevectors.

4. Neutron diffraction

The present experiment makes use of a combination of high flux (D1B, $\lambda = 2.52$ Å, 2θ: ($0° \to 80°$), step increment of 0.20°) and high resolution (D1A, $\lambda = 1.9108$ Å and $\lambda = 2.99$ Å, 2θ: ($0° \to 160°$), step increment of 0.10°)

data. The D1B data are used to derive the phase diagram on heating and cooling with a 0.1 K temperature step in the range 1.2 K $\to$ 15 K; see section 4.1.2.

The high resolution D1A data collected with a larger wavelength (2.99 Å) and very good statistics provide the best resolved magnetic patterns and are therefore used for detecting the magnetic wavevector(s) and higher harmonics and resolving the large number of overlapping magnetic peaks. There are also used in magnetic refinements. The eighteen data sets are partly collected with a temperature step of 0.1 K over the transition regions along the lines of the specific heat and magnetization measurements.

The 1.9108 Å D1A data with the large 2θ range are used for eight selected temperatures for indexing of the magnetic reflections (i.e. figure 5) and simultaneous structural and magnetic refinements in order to check for possible structural transitions in the high angle part. The data analysis is done with the *FullProf Suite* of programs [10]. The structure plots are made with the program FullProf Studio [11] incorporated in [10]. Results are given in the following sections.

Preliminary neutron diffraction data were collected for a HoGe$_3$ sample (I) with the G4.1 (800-cell position sensitive detector (PSD)) at the Orphée reactor (LLB-Saclay), $\lambda = 2.426$ Å, 2θ:($3° \to 83°$) and step increment of 0.10° for a few temperatures and with the DMC multicounter system at the reactor Saphir, Würenlingen ($\lambda = 1.7008$ Å, 2θ:($0° \to 135°$) and step increment of 0.10°), for 1.5 and 35 K. The refined paramagnetic data confirm the structure and the sample purity while the indexing of the LT data led us to an unsolvable situation of a 40-times larger cell ($5a, 2b, 4c$). The G4.1 neutron diffraction data cannot be used for quantitative analysis due to (a) the high complexity of the magnetic patterns, (b) the limited 2θ range and (c) the presence of two impurity lines from the cryostat. However they provide first information for a complex magnetic phase diagram and serve to trace the present experimental strategy for sample (II) together with the specific heat and magnetization results.

4.1. Model independent information

4.1.1. Structural refinements, D1A, 1.9108 Å data. The structural refinements in the paramagnetic state at 14 K confirm the DyGe$_3$ type of structure and the sample purity. There is a minor non-overlapping unidentified impurity (i) line around $2\theta \approx 33°$ (see figure 5). The results obtained at various temperatures in the magnetically ordered regime confirm that the structure remains stable down to 1.8 K and that the magnetic transitions are not accompanied by significant structural changes, which is important in view of the indexing of the LT complex magnetic patterns as we can refer to the same HT basis. This can be seen by comparing the high angle region of the 10.28 K pattern included in figure 5 (bottom part) that displays the simplest magnetic peak topology. The refined structural parameters are summarized in table 1. The agreement factors are satisfactory. Details concerning the refinement of the 10.28 K magnetic phase are given in table 1 of part II of the paper together with other data of the HT range after the model choice. Furthermore our data reproduce the
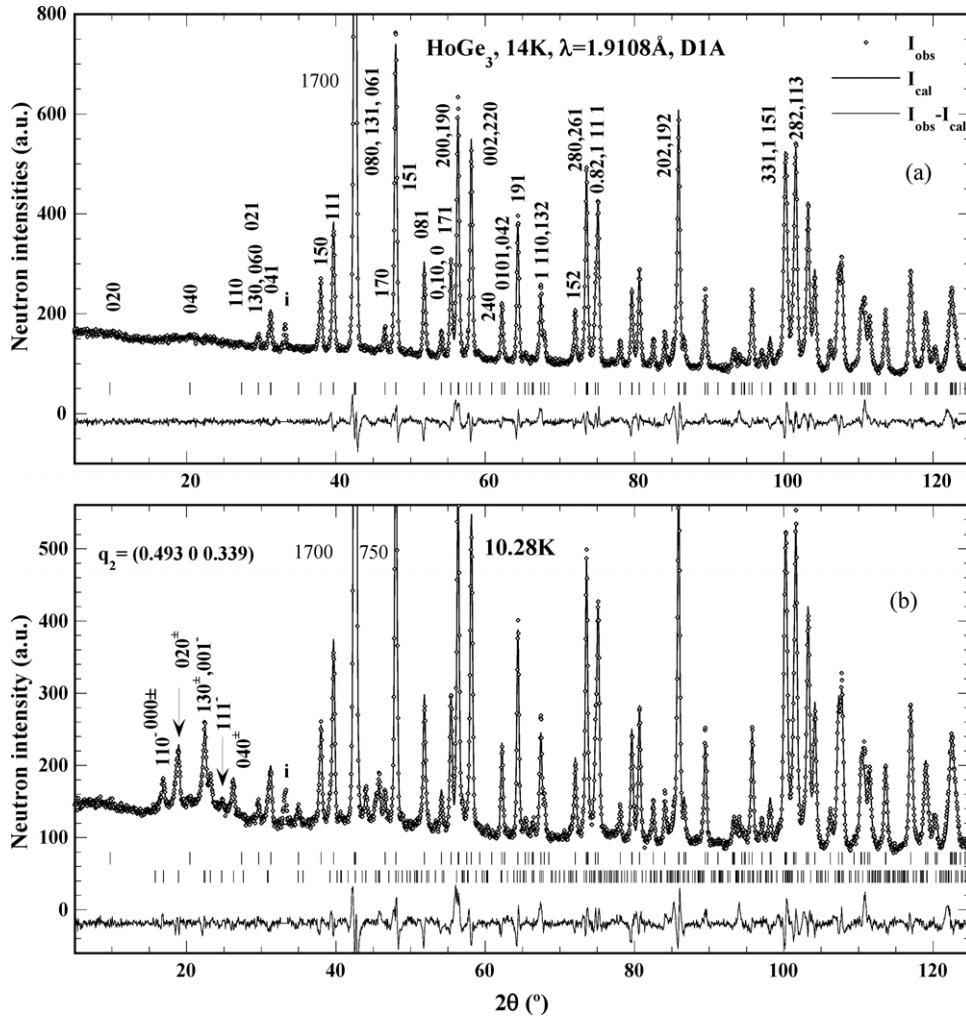
Figure 5. Parts of the observed and calculated neutron diffraction patterns of HoGe$_3$: (a) in the paramagnetic state at 14 K, (b) in the HT magnetically ordered state at 10.28 K with $q_2 = (q_{2x}, 0, q_{2z}) \approx (\frac{1}{2}, 0, \frac{1}{3})$ referring to the C-cell (on a 1.25-times enlarged vertical scale).

Table 1. Refined structural parameters of HoGe$_3$ from neutron diffraction data ($\lambda = 1.9108$ Å) for the (i) paramagnetic state at 14 K and (ii) magnetically ordered state. Space group $Cmcm$ (No 63); all atoms at 4c: (0, y, $\frac{1}{4}$).

		14 K	10.28 K	9.315 K	8.34 K	3.47 K	1.7 K
Atom	x	y	y	y	y	y	y
Ho	0.0	0.4168(1)	0.4170(1)	0.4170(1)	0.4170(1)	0.4169(1)	0.4167(1)
Ge(1)	0.0	0.0394(1)	0.0394(1)	0.0394(1)	0.0393(1)	0.0393(1)	0.0395(1)
Ge(2)	0.5	0.1909(1)	0.1910(1)	0.1908(1)	0.1909(1)	0.1912(1)	0.1912(1)
Ge(3)	0.5	0.3106(1)	0.3106(1)	0.3107(1)	0.3107(1)	0.3103(1)	0.3104(1)
B (Å)^2	0.18(3)		0.12(3)	0.03(3)	0.06(3)	0.28(3)	0.08(3)
a (Å)	3.9897(1)		3.9899(1)	3.9915(1)	3.9916(1)	3.9894(1)	3.9898(1)
b (c)	20.6882(2)		20.6888(2)	20.6976(2)	20.6984(2)	20.6884(3)	20.6895(3)
c (Å)	3.8795(1)		3.8793(1)	3.8809(1)	3.8809(1)	3.8791(1)	3.8793(1)
R_B, R_{wp}%	3.6, 12		3.4, 11.9	2.9,11.3	2.8, 11.3	2.8, 12.6	3.5, 13.6
R_{exp}%, χ^2	5.8, 4.2		5.7, 4.4	5.4, 4.3	5.3, 4.8	4.4, 8.3	3.4, 15.8

findings for sample (I) concerning the magnetic transitions at any temperature.

4.1.2. Magnetic phase transitions from D1B data. The D1B thermodiffractograms shown in figures 6(a) (2D plot on heating and cooling) and (b) (3D plot on cooling) display a succession

of phase transitions below the magnetic ordering temperature $T_N \approx 11$ K with increasing complexity as the temperature goes down. In the displayed low 2θ angle part the nuclear intensities have negligible contribution. Therefore the large number of magnetic peaks and their thermal behaviour reflect the interplay of competing magnetic orderings. The structural parameters obtained from the refinements of the high 2θ angle
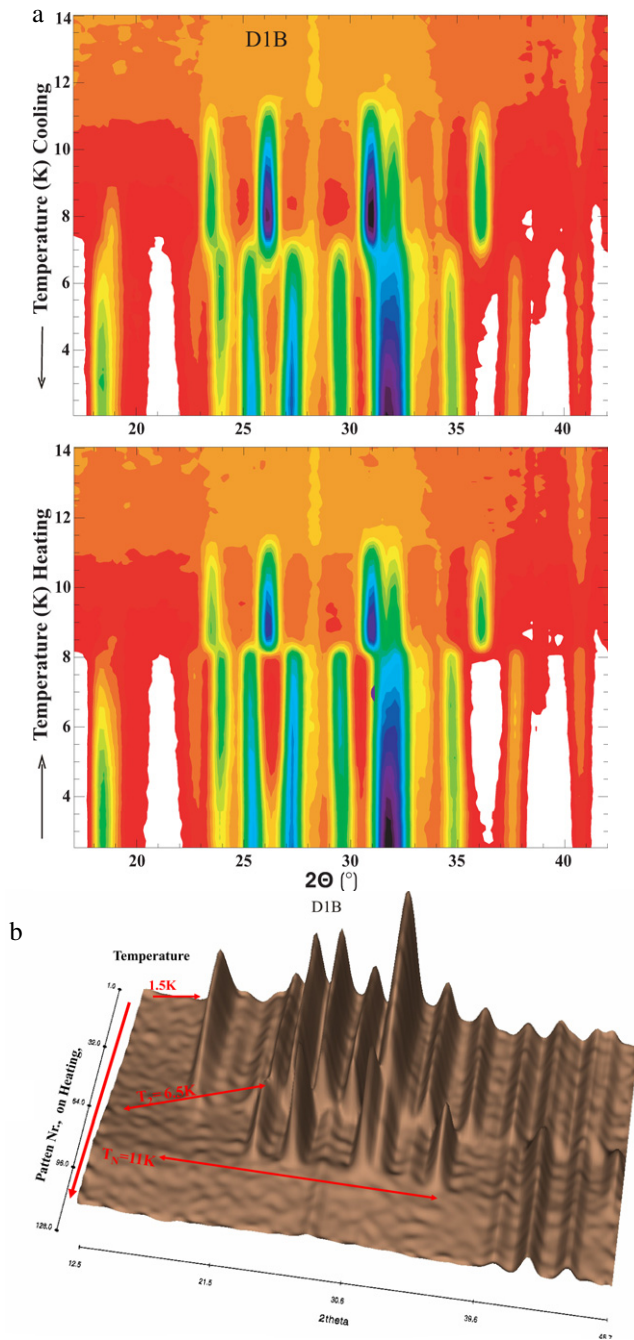
Figure 6. Thermodiffractogram of HoGe$_3$: (a) in a 2D projection on heating and cooling showing the succession of magnetic phase transitions below $T_N = 11$ K at $T_2^H = 8.1$ K and $T_3^H = 4.8$ K (temperatures given on heating) and (b) in a 3D view on cooling.

of the D1A data in the previous section show no structural changes to be present within the experimental error. Therefore the indexing of the new peaks refers to the same orthorhombic *C*-cell. The thermal behaviour of the various phases on cooling and heating (see figure 6(a)), based on the neutron data analysis given in the following sections, provides a first description of the observed successive transitions below the Néel transition and of their characteristics. This information is then completed successively by the refined parameters of the models that led to the best fit.

4.1.2.1. Major transitions, T_N (second order), T_2 (first order). The most important step in the data analysis is the detection of the magnetic wavevectors [12]. Figure 6(a) shows clearly that long range ordering appears for both data sets (cooling and heating) at $T_N = 11$ K and that the Néel transition is of second order. Furthermore it shows two major ranges of magnetic order besides the paramagnetic state, namely the HT range spanning between $T_N = 11$ K and $T_2^H = 8.1$ K and the LT range between 1.8 K and T_2. The temperatures refer to the values obtained on heating (figure 6(a), bottom part). A hysteresis width of about 1.5 K found for the T_2 transition between heating ($T_2^H = 8.1$ K) and cooling ($T_2^C = 6.6$ K) and the coexistence of the HT and LT phases around T_2 suggest a first-order transition. The T_2^H transition temperature and the hysteresis effects are confirmed also by the magnetization measurements in figure 4(b), while the broad peak on cooling does not enable the exact estimation of the T_2^C temperature from these data. We would like to note that this transition temperature was tentatively assigned to the tiny anomaly found in the specific heat at ≈ 6.6 K in figure 4(c) in section 3.2.

4.1.2.2. Minor transitions, T_1, T_3. A closer inspection of the patterns shows additional subtle changes not distinguishable from the background in figure 6(a) due to the noise filter of the plot program. One is found in the LT range at $T_3^H = 4.8$ K (on heating). We show this transition by comparing the better resolved 5.35 K and 1.5 K D1A $\lambda = 2.99$ Å data in figure 7. The relative magnetic peak intensities have changed and also minor positional changes are observed. Details concerning the positional change are given in section 4.1.4c and in figure 11. The indexing given in the figure anticipates the results presented in the following section. These facts point to minor magnetic structural changes and subdivide the low temperature range into the ranges LT$_1$ (1.8 K $\rightarrow$ T_3) and LT$_2$ (T_3 $\rightarrow$ T_2). The second transition is suggested by a small anomaly in the specific heat and C/T at $T_1 \approx 9.5$ K in figure 4(a) and the derivative of the magnetization figure 4(b). This point is addressed in conjunction with the indexing of the HT phase and possible participation of the wavevector q_1 (see section 4.1.4a).

4.1.3. Indexing, D1A data.

4.1.3.1. The HT and IT ranges $T_2 \rightarrow T_N$ (q_1, q_2). The HoGe$_3$ HT and IT magnetic peak topology resembles that of TbGe$_3$ HT and the indexing is straightforward as can be seen from figure 8, comparing the TbGe$_3$ 27 K data with the 10.28 and 7.37 K HoGe$_3$ data (D1A 1.91 Å data) in a $\sin\theta/\lambda$ scale representation. The strongest observed magnetic reflections appearing below $T_N = 11$ K in HoGe$_3$ are located around the 2θ positions (020) $\pm q_2$ and (130) $- q_2$, like for TbGe$_3$. We therefore assign them to the same wavevector, $q_2 = (q_{2x}, 0, q_{2z})$. These two reflections as well as the full set of magnetic peaks are indexed by a single incommensurate wavevector with temperature variable length $q_{2x} \approx \frac{1}{2}$ and $q_{2z} \approx \frac{1}{3}$. A very weak reflection appearing at slightly lower temperature has, by the analogy to TbGe$_3$, tentatively been assigned to the wavevector $q_1 = (q_{1x}, 0, 0)$. The 7.37 K data
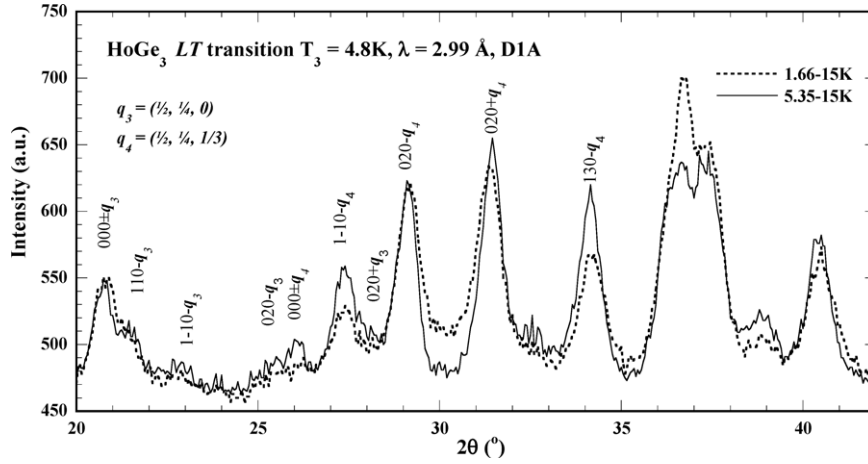
Figure 7. The low angle part of D1A (2.99 Å) neutron patterns showing subtle changes of the magnetic intensities in the LT range above and below the transition temperature $T_3^H = 4.8$ K.
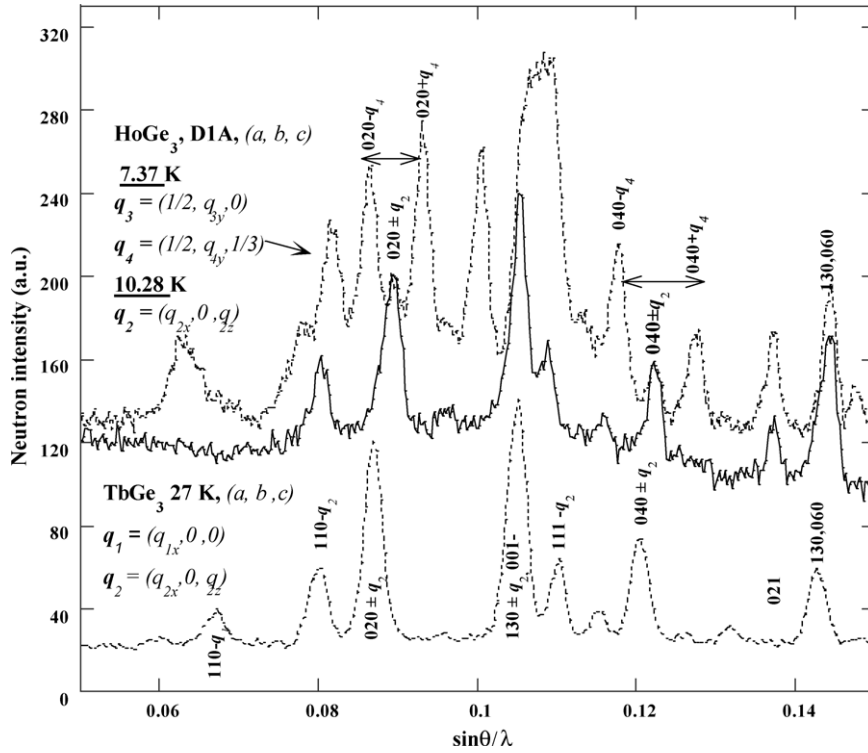

Figure 8. A characteristic part of the HT (27 K) TbGe$_3$ neutron diffraction pattern associated with the wavevectors $q_1 = (q_{1x}, 0, 0)$ and $q_2 = (q_{2x}, 0, q_{2z})$, $q_{1x} \neq q_{2x} \approx \frac{1}{2}$ and $q_{2z} \approx \frac{1}{3}$. The pattern of the isomorphic HoGe$_3$ at 10.28 K (HT phase) displays the same peak topology for the wavevector q_2 in TbGe$_3$. At 7.37 K two new vectors, $q_3 = (\frac{1}{2}, q_{3y}, 0)$ and $q_4 = (\frac{1}{2x}, q_{4y}, \frac{1}{3})$, $q_{3y} \approx \frac{1}{4}$ and $q_{4y} \approx \frac{1}{4}$, appear at the cost of the q_2 vector, which fully disappears.

consist of a mixture of phases. A small portion pertains to the (q_1, q_2) HT phase and the LT phase discussed below.

4.1.3.2. The LT range $1.8 \ K \rightarrow T_2 \ (q_3, q_4)$. The LT indexing follows on analysing the positional shift experienced by several magnetic satellites in figure 8 between the 10.28 and 7.37 K data. One may draw the following simple conclusion. The intensity of the satellites of axial reflections such as $(0k0) \pm q_2$ as $(020) \pm q_2$, $(040) \pm q_2$ decreased strongly as the temperature decreased to 7.37 K. On the other hand, the central reflection

persisted and was decorated by two strong almost equidistant satellites pertaining to a new wavevector q. The almost symmetrical splitting of these reflections at 7.37 K suggests the existence of a wavevector component along the b axis q_y, as any change of the q_{2x} or q_{2z} components would only result in a positional shift and not in a splitting. The starting value of the q_y component can be estimated by means of the relation

$$d^{*2} = 4\sin^2\theta/\lambda^2 = (h \pm q_x)^2 a^{*2} + (k \pm q_y)^2 b^{*2}$$
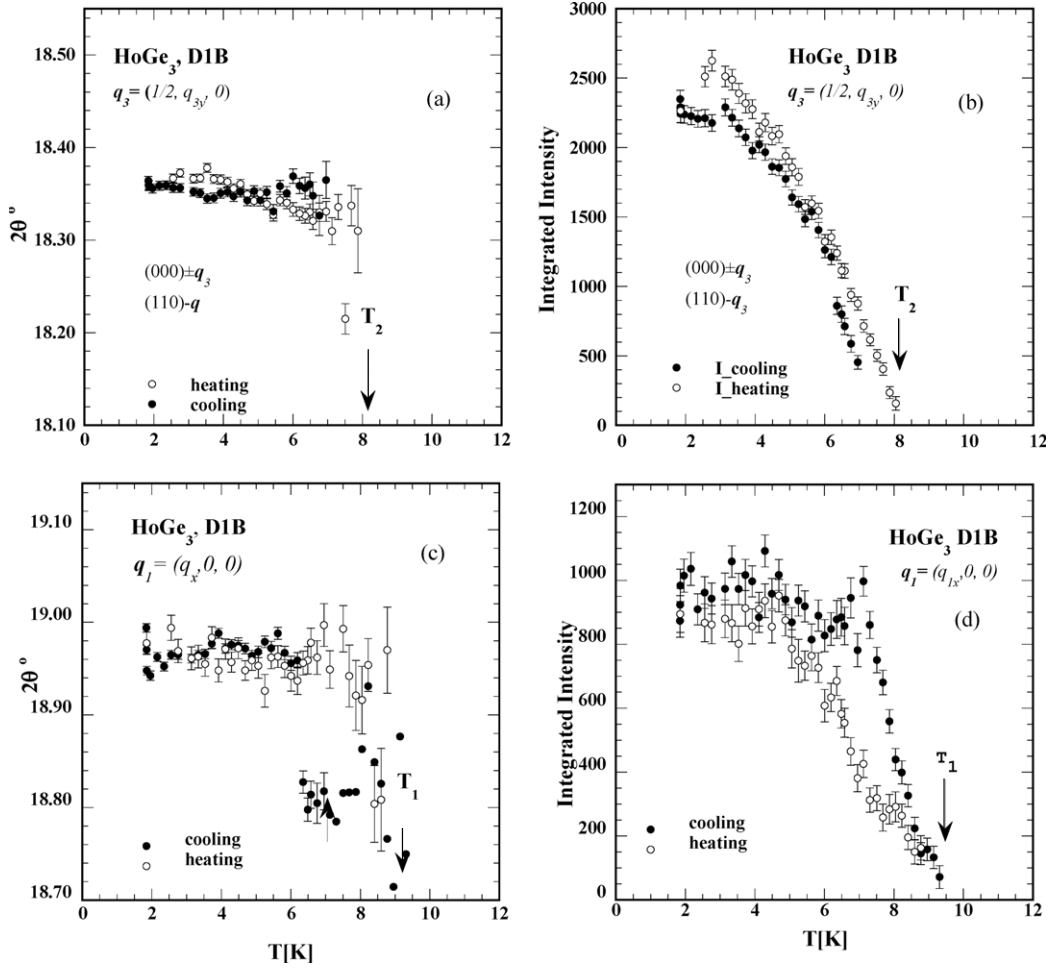$$+ (l \pm q_z)^2 c^{*2} \tag{1}$$

Figure 9. Thermal variation of the 2θ positions and the magnetic intensities $((000) \pm q_3$ and $(110) - q_3)$ and $(1\bar{1}0) - q_1$ located at the lowest 2θ angle pertaining to the wavevectors $q_3 = (\frac{1}{2}, q_{3y}, 0)$ with $q_{3y} \approx \frac{1}{4}$ ((a) and (b)) and for the wavevector $q_{1z} = (q_{1x}, 0, 0)$, $q_{1x} \approx \frac{1}{2}$ ((c) and (d)) in HoGe$_3$ intermediate temperature (IT) and LT ranges (D1B data on heating and cooling).

q_y can be obtained by subtracting the $\sin^2 \theta$ values of the satellites $((040) \pm q_2) - q$ and $((040) \pm q_2) + q$; the corresponding 2θ values are $26.113°$ and $28.248°$:

$$q_y = (\sin^2 \theta_{(040)+} - \sin^2 \theta_{(040)-})b^2/4\lambda^2 = 0.2494. \quad (2)$$

Within the experimental error the wavevector has a commensurate value $q = (\frac{1}{2}, \frac{1}{4}, \frac{1}{3})$ and the HoGe$_3$ neutron data can be indexed in various ways: (i) with a commensurate 24-times larger cell $(2a, 4b, 3c)$ or alternatively with a modulated structure: (ii) an (a, b, c) C-cell with two wavevectors $q_3 = (\frac{1}{2}, \frac{1}{4}, 0)$ and $q_4 = (\frac{1}{2}, \frac{1}{4}, \frac{1}{3})$ or (iii) a six-times larger P-cell $(2a, b, 3c)$ and a single wavevector $q = (0, \frac{1}{4}, 0)$. The indexing of the LT magnetic data with any of these cells was straightforward at all temperatures. The first case for $\lambda = 1.91$ Å produces a huge number of reflections. Refinements were undertaken for the latter two cases. The (q_3, q_4) model produces about 1330 reflections while the other produces 7930. In the 1.91 Å data the reflection positions of the LT magnetic phase do not display significant changes with temperature. As it is only their intensity that increases going down with temperature, our primary assumption is that the LT phase is commensurate with the crystal lattice. A careful observation

of the D1B data in figure 6(a) indicates that at least two of the satellites around 26° are moving closer below 5 K (on heating). A more precise explanation of these changes is given in later sections on the basis of the 2.99 Å data.

4.1.4. Thermal behaviour of the magnetic satellites. The thermal behaviour of the magnetic intensities pertaining to the various wavevectors observed in HoGe$_3$ is followed on cooling and heating (D1B data). The behaviour of the strongest intensities of each vector set is depicted in figures 9–11: for $q_1 = (q_{1x}, 0, 0)$, $q_3 = (\frac{1}{2}, \frac{1}{4}, 0)$ in figure 9, for $q_2 = (q_{2x}, 0, q_{2z})$ in figure 10 and for $q_4 = (\frac{1}{2}, \frac{1}{4}, \frac{1}{3})$ in figure 11. All vectors refer to the conventional C-cell.

This information is obtained by deconvolution of the selected reflections in the low 2θ angle range of the D1B data (figure 6(a)) using the 'FIT' tool of the program [10] while the thermal variation of the wavevector components were obtained by using the 'profile matching tool'. As already said, the indexing of the reflections is based on the HR 2.99 Å D1A data fits (see section 4.1.3) while the behaviour of the LT magnetic vectors became available only after the final refinements that will be presented in part II (see also figure 6). Here we would
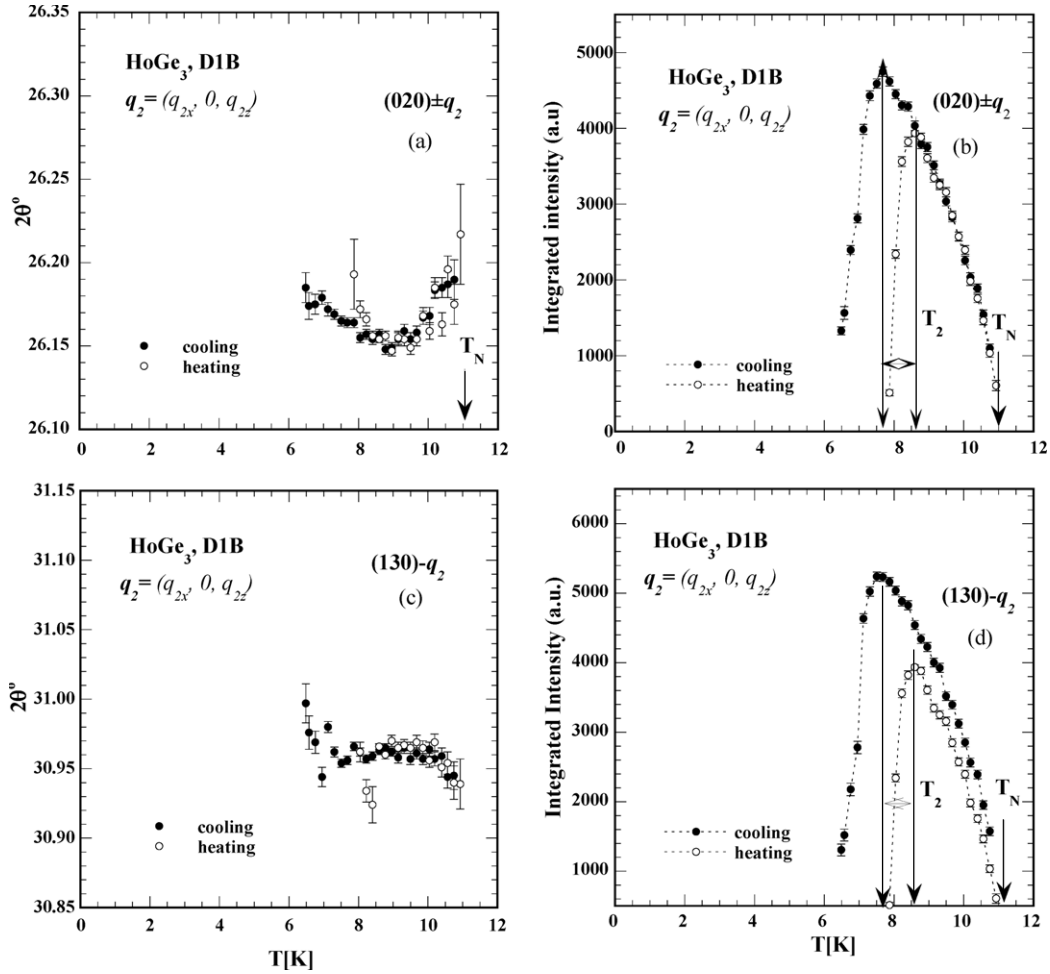
Figure 10. Thermal variation of the 2θ positions and magnetic intensity of the satellites $(020) \pm q_2$ ((a) and (b)), $(130) - q_2$ ((c) and (d)) respectively, $q_2 = (q_{2x}, 0, q_{2z})$ with $q_{2x} \approx \frac{1}{2}$, $q_{2z} \approx \frac{1}{3}$ in HoGe$_3$ (D1B data, heating and cooling).

like to state that selecting the $(q_3, q_4)LT$ phase description, that produces the minimum number of satellites, does not impose any limitations to the LT model choice.

4.1.4.1. $q_1 = (q_{1x}, 0, 0)$ *and* $q_3 = (\frac{1}{2}, \frac{1}{4}, 0)$ *satellites.* Figure 9 shows the thermal evolution of the very weak magnetic intensities located at the lowest 2θ angle around $18.5°$ (D1B data). It relates to the identification of the q_1 and q_3 vectors and their interplay. Below $T_1 = 9.5$ K a very weak peak appears at $2\theta = 18.8°$ close to the position $(\frac{1}{2}, 1, 0)$. This peak is visible in the 1.9108 Å data but not in the 2.99 Å data where it is smeared by the $\lambda/3$ contribution of 1% of the strongest nuclear peak (131). In view of the similarity with TbGe$_3$ this peak pertains to the incommensurate HT (q_1, q_2) phase with $q_1 = (q_{1x}, 0, 0)$ and $q_2 = (q_{2x}, 0, q_{2z})$. Unlike the findings in TbGe$_3$ the 2θ position of this unique observation $(110) - q_1$ is not temperature dependent; see figure 9(c). Its intensity rises below 9.5 K and continues to increase down to 4 K; see figure 9(d). But as discussed in section 5 its inclusion in the D1A 1.91 Å refinements is questionable.

We consider here two possibilities concerning the nature of q_1. One is that q_1 does not belong to the HT HoGe$_3$ magnetic structure and most likely relates to the ordering of the unidentified impurity phase. The second is that q_1 jumps

to the $q_3 = (\frac{1}{2}, \frac{1}{4}, 0)$ value simultaneously with the transition $q_2 \to q_4$ at the lock-in temperature T_2. The latter assumption is supported by the fact that just below $T_2^H = 8.1$ K one observes a broadening of the $(110) - q_1$ peak and the simultaneous appearance of at least one additional peak at $2\theta = 18.35°$ on the left side of $(110) - q_1$. According to the more reliable analyses of the HR D1A 2.99Å LT data based on the simplest (q_3, q_4) model, this double peak is indexed as $(000) \pm q_3$ and $(1\bar{1}0) - q_3$ with $q_3 \approx (\frac{1}{2}, \frac{1}{4}, 0)$ (see figure 7 and section 4.1.4c for indexing). These two peaks are almost unresolved in the D1B data and their position and intensity variation are shown as a single observation in figure 9 (upper part). The deconvolution of close very weak peaks especially in the transition region is a difficult task and may lead to artefacts in view of the large errors; the peak around 7 K in figure 9(d) on cooling ($(110) - q_1$ intensity variation) is certainly an artefact. Therefore the quantities displayed in figure 9 have to be treated with some reservation. Within the experimental error the position of the q_1 peak remains unchanged while its intensity increases smoothly down to 1.8 K (see figure 9(c), on heating). This could indicate that q_1 relates to the impurity phase. However, the missing information concerning the q_1 behaviour at T_2 and the simultaneous occurrence of the unresolved q_3 Fourier coefficients leave the possibility open
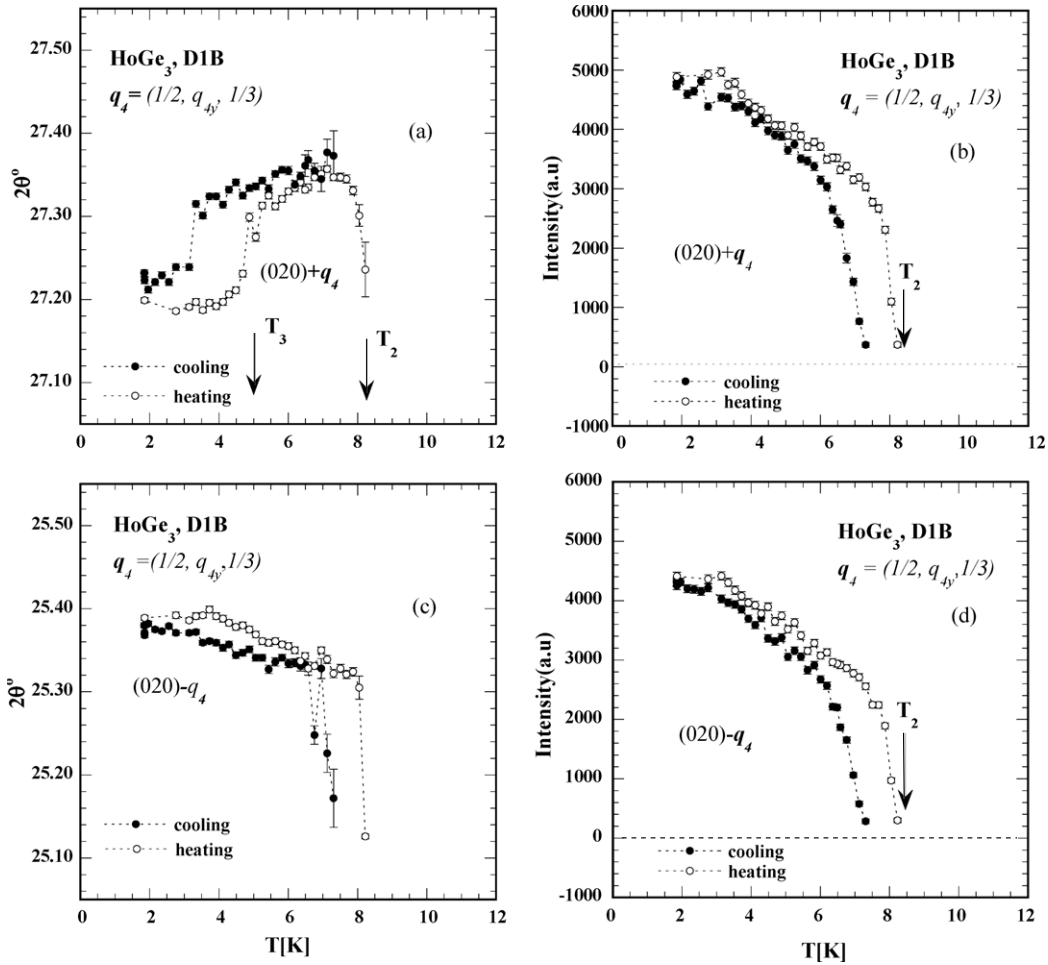
Figure 11. Thermal variation of the 2θ positions and magnetic intensity of the satellites $(020) + q_4$ ((a) and (b)) and $(020) - q_4$ ((c) and (d)) respectively, $q_4 = (q_{4x}, q_{4y}, \frac{1}{3})$ with $q_{4x} \approx \frac{1}{2}$, in HoGe$_3$ (D1B data, heating and cooling).

that q_1 contributes to the HT (q_1, q_2) ordering in HoGe$_3$ and jumps to q_3 below T_2.

The ambiguity concerning the nature of q_1 and the interplay of q_1, q_3 at low angles might be resolved experimentally, either with single-crystal data (in spite of several efforts not being currently available), or using HR powder data with even larger wavelength than $\lambda > 3$ Å (without $\lambda/3$ contamination) and better statistics than our present data.

4.1.4.2. $q_2 = (q_{2x}, 0, q_{2z})$ satellites (HT). Figure 10 shows the thermal behaviour of the strongest q_2 satellites $(020) \pm q_2$ around $2\theta \approx 26.1°$ and $(130) - q_2$ around $2\theta \approx 31°$ (D1B data). Figure 10(a) shows that the position of the $(020) \pm q_2$ satellite varies non-monotonically with temperature. We then can assume that the q_2 length and direction are changing with temperature. From the intensity changes (on heating and cooling) one can draw the conclusion that the Néel transition is of second order. Its intensity increases smoothly from T_N down to $T_2^H = 8.1$ K where it reaches its maximum value. Below this temperature it suddenly disappears via a first-order transition and a large number of magnetic reflections associated with the wavevectors q_3 and q_4 become visible as a decoration of the q_2 set. The (q_3, q_4) sets become more

important at lower temperatures at the cost of the q_2 set, which fully disappears. We note that the thermal variation of the q_2 wavevector components was obtained from the final refinement of the D1A data, which we will present in part II of the paper in conjunction with a model choice for the transition mechanism.

4.1.4.3. $q_4 = (\frac{1}{2}, q_{4y}, \frac{1}{3})$ satellites (LT). The thermal behaviour of the best resolved LT satellites of the wavevector $q_4 = (\frac{1}{2}, q_{4y}, \frac{1}{3})$ (see figure 7), $(020) - q_4$ and $(020) + q_4$, are given in figure 11. Both satellites appear suddenly below ≈ 8.3 K (on the heating curve) via a first-order transition at the cost of the q_2 HT reflections. Their intensity rises fast between 8.3 and 7.3 K and then changes slope and increases down to 3 K where it reaches saturation. As the intensity of the q_4 satellites increases at the cost of the q_2 satellites the transition temperature T_2^H or T_2^C is defined at the intersection of the corresponding curves; see figure 12 (lower part). In the range 5 K $\rightarrow$ 8.1 K below T_2^H the 2θ angles of the $(020) - q_4$ and $(020)+q_4$ satellites vary slightly in opposite directions: the former to slightly higher 2θ angles and the latter to lower 2θ. This fact suggests a decrease of the q_{4y} component going down with temperature. Below the LT transition at $T_3^H = 4.8$ K a 2θ discontinuity is observed only for the $(020) + q_4$ reflection; see figure 11(a). Surprisingly this discontinuity is not visible in

the $(020) - q_4$ plot (figure 11(c)). One may suggest that this is related to the simultaneous appearance of additional Fourier coefficients unresolved from $(020) + q_4$ even in the 2.99 Å data but related to the commensurate structure. The $(020) + q_4$ peak intensity has a slight decrease while a more important decrease is seen for adjacent peaks such as $(1\bar{1}0) - q_4$ and $(130) - q_4$ in figure 7. Such details point to the interplay of various vectors related to modifications such as spin reorientation of the magnetic structure. First information might again be found using data collected with an even larger wavelength and high resolution, and statistics better than the present ones. However refinements of large cells need a much larger $\sin\theta/\lambda$ range.

5. Concluding remarks

In the present part of our paper (part I) we have focused on the presentation of the experimental results of the investigation. The use of various neutron data sets and the physical properties in the study of the magnetic transitions occurring in the HoGe$_3$ compound led to a rather complex temperature magnetic phase diagram shown in figure 12. The succession of phases is presented in terms of wavevectors. This information is extracted from the thermal behaviour of a full set of magnetic neutron intensities (high flux data) within the low range ($3° \rightarrow 45°$) 2θ angle. It is based on the peak position shift and the intensity variation in the temperature range 1.8 K $\rightarrow$ 11 K on heating and cooling.

The various wavevectors are identified by indexing the high resolution D1A data for selected temperatures by the 'profile matching' program tool over the entire 2θ range, which is model independent. Their interplay is schematically shown in the top part of figure 12. The phase diagram comprises besides the second-order Néel transition three further transitions at $T_1 = 9.5$ K, $T_2 = 8.1$ K, $T_3 = 4.8$ K (on heating). The T_2 transition is of first order. The most reliable transition temperature values are those obtained from the neutron data analysis. An effort is made throughout the text to bring them into relation with the subtle anomalies displayed in the specific heat and the magnetic measurements.

In the low part of the graphic presentation we include the integrated intensity variation (on heating and cooling, D1B HI data) of two characteristic resolved magnetic reflections, one pertaining to the HT regime $(020) \pm q_2$ with $q_2 = (q_{2x}, 0, q_{2z})$ the other to the LT regime $(020) - q_4$ with $q_4 = (\frac{1}{2}, \frac{1}{4}, \frac{1}{3})$. This allows a direct derivation of the main characteristics of the phase diagram such as the T_2 temperature and of hysteresis effects. The temperatures T_2^H and T_2^C are defined at the intersection of the two relevant intensity curves on heating and cooling respectively. Under the experimental conditions (heating/cooling speed) for the neutron data the hysteresis of the T_2 transition has a width of 1.5 K. Furthermore the phase diagram shows the coexistence region(s) of the adjacent phases as defined experimentally. These are displayed as shadowed ranges around the first-order transition T_2 beginning at the lowest temperature ($T < T_2$) where the HT phase is observed as a metastable phase, and ending at the highest temperature ($T > T_2$) where the LT phase exists as a metastable phase. Under the present experimental conditions the coexistence
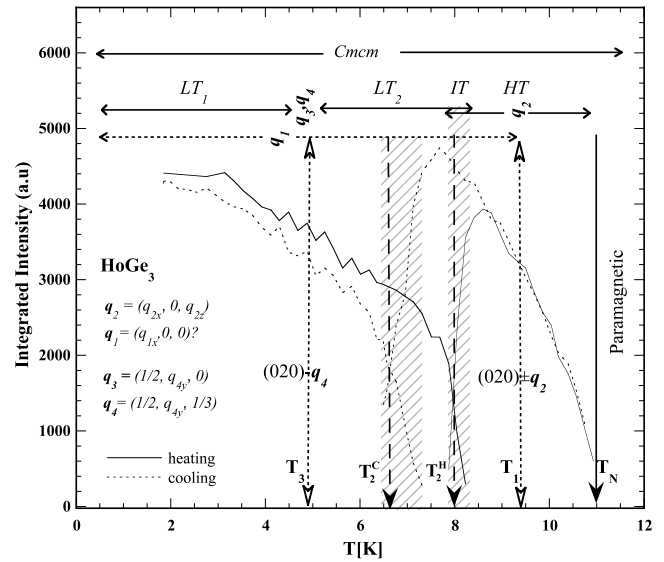

Figure 12. The magnetic phase diagram of HoGe$_3$, showing the interplay of the four wavevectors $q_1 = (\frac{1}{2}, 0, 0)$, $q_2 = (q_{2x}, 0, q_{2z})$, $q_3 = (\frac{1}{2}, q_{3y}, 0)$ and $q_4 = (\frac{1}{2}, q_{4y}, \frac{1}{3})$ (upper part) with temperature. Included is the intensity variation of $(020) - q_4$ and $(020) \pm q_2$ (D1B data on heating and cooling) allowing a direct detection of the coexistence range, hysteresis effects and the transition temperatures: $T_N = 11$ K (full line: second-order transition), $T_2^H = 8.1$ K on heating (discontinuous vertical line: first-order transitions). Two minor transitions at $T_1 = 9.6$ K (appearance of q_1) and at $T_3^H = 4.8$ K (dashed lines) structural changes in the LT (q_3, q_4) magnetic phase are extracted from other observations (lock-in transition). The shadowed ranges around 8.1 and 6.6 K are the coexistence ranges of the adjacent HT and LT phases across the first-order transition at T_2 on heating and cooling respectively.

range around T_2^C (on cooling) is 0.8 K, which is larger than 0.5 K found around T_2^H (on heating).

Further details concerning the wavevectors q_1, q_3 and minor transitions at T_1 and T_3, displayed as dashed lines with open arrows, are added from other observations and discussed. T_1 relates to the appearance of the q_1 vector in the HT range (section 4.1.4a) below 9.6 K, while $T_3^H = 4.8$ K relates to a lock-in transition of the q_{4y} and q_{3y} components, most probably connected to a spin reorientation and to the appearance of additional Fourier coefficients below T_3. This latter point is not yet fully clarified in the present paper. This transition is most probably of first order as the heating and cooling intensities are relatively shifted in the range 4.8 K down to 1.8 K. Unlike for the T_2 transition the coexistence range of the incommensurate and the lock-in phase cannot be derived from our data due to strong peak overlap. That is why no shadowed ranges are shown around T_3. Details concerning the transition mechanisms might be addressed after the model dependent refinements of the relevant magnetic structures and will be given in part II of our paper.

The magnetization and specific heat measurements confirm the Néel transition temperature $T_N = 11$ K obtained from the neutron results and that this transition is of second order. The transitions found from the neutron data analysis at $T_1 \approx 9.5$ K and $T_2^H = 8.1$ K, $T_2^C = 6.6$ K could be brought into relation with the specific heat and the magnetization

measurements. The T_2 transition is of first order and its value obtained from neutron data obtained on cooling relates to that of the specific heat anomaly around 6.6 K obtained on cooling. The lock-in transition at $T_3^H = 4.8$ K is only observed in the neutron data. As already mentioned, the refinements of the magnetic structures are model dependent and will be given in a separate part (part II) of the paper in view of the high complexity of the phase diagram.

References

[1] Schobinger-Papamantellos P, de Mooij D B and Buschow K H J 1992 *J. Alloys Compounds* **183** 181

[2] Schobinger-Papamantellos P, Rodriguez-Carvajal J, Janssen T and Buschow K H J 1994 *Conf. Proc. 'Aperiodic 94' (Les Diablerets)*

[3] Schobinger-Papamantellos P, André G, Rodríguez-Carvajal J and Buschow K H J 1996 *J. Alloys Compounds* **232** 165

[4] Schobinger-Papamantellos P, Janssen T and Buschow K H J 1996 *J. Magn. Magn. Mater.* **154** 29

[5] Schobinger-Papamantellos P, Rodriguez-Carvajal J and Buschow K H J 2007 *J. Phys.: Condens. Matter* **19** 236201

[6] Schobinger-Papamantellos P and Buschow K H J 1988 *J. Less-Common Met.* **139** 221

[7] Belyavina N M, Markiv V Ya and Speka M V 1992 *J. Alloys Compounds* **283** 162–8

[8] Wei M S, Sung H H and Lee W H 2005 *Physica* C **424** 25

[9] Abert K, Meyer H J and Hoffmann R 1993 *J. Solid State Chem.* **106** 201

[10] Rodríguez-Carvajal J 1993 *Physica* B **192** 55 The programs of the *FullProf Suite* and their corresponding documentation can be obtained from the Web at http://www.ill.eu/sites/fullprof/.

[11] Chapon L C and Rodríguez-Carvajal J 2005 unpublished *FullProf Studio* is a program of the *FullProf Suite* the most recent version is freely available in the site given in [10]

[12] Rossat-Mignod J 1987 *Methods of Experimental Physics: Neutron Scattering* vol 3 (New York: Academic)